Improved characterization of heterogeneous permeability in saline aquifers from transient pressure data during freshwater injection

Peter K. Kang[*, 1, 2], Jonghyun Lee[*, 3], Xiaojing Fu[2], Seunghak Lee[1], Peter K. Kitanidis[3], and Ruben Juanes[2,4]

* Peter K. Kang and Jonghyun Lee contributed equally to the manuscript.

Key Points:

- Efficient subsurface imaging methodology is proposed for saline aquifer characterization
- Transient pressure data in variable density flow provides robust information for subsurface characterization
- Inversion accuracy increases as density contrast between the injected and ambient fluids increases

Corresponding author: S. Lee, Korea Institute of Science and Technology, Seoul 136-791, Republic of Korea. (seunglee@kist.re.kr)

[1]Korea Institute of Science and Technology,

Abstract. Managing recharge of freshwater into saline aquifers requires accurate estimation of the heterogeneous permeability field for maximizing injection and recovery efficiency. Here, we present a methodology for subsurface characterization in saline aquifers that takes advantage of the density difference between the injected freshwater and the ambient saline groundwater. We combine high resolution forward modeling of density-driven flow with an efficient Bayesian geostatistical inversion algorithm. In the presence of a density difference between the injected and ambient fluids due to differences in salinity, the pressure field is coupled to the spatial distribution of salinity. This coupling renders the pressure field transient: the time evolution of the salinity distribution controls the density distribution which then leads to a time-evolving pressure distribution. We exploit this coupling between pressure and salinity to obtain an improved

Seoul 02792, Republic of Korea

[2]Department of Civil and Environmental Engineering, Massachusetts Institute of Technology, Cambridge, Massachusetts, USA.

[3]Department of Civil and Environmental Engineering, Stanford University, Stanford, California, USA

[4]Department of Earth, Atmospheric and Planetary Science, Massachusetts Institute of Technology, Cambridge, Massachusetts, USA.

characterization of the permeability field without multiple pumping tests or additional salinity measurements. We show that the inversion performance improves with an increase in the mixed convection ratio—the relative importance between viscous forces from injection and buoyancy forces from density difference. Our work shows that measuring transient pressure data at multiple sampling points during freshwater injection into saline aquifers can be an effective strategy for aquifer characterization, key to the successful management of aquifer recharge.

1. Introduction

As world population continues to rise at an unprecedented rate, water demand is surpassing supply in many areas of the world [*Rijsberman*, 2006]. Climate change will only expose many more regions to water shortage issues in the near future [*Vörösmarty et al.*, 2000]. As a major water supply source, groundwater is depleting at an alarming rate due to overexploitation, and saline aquifers are becoming more and more common as seawater intrusion aggravates [*Aeschbach-Hertig and Gleeson*, 2012; *Gleeson et al.*, 2012; *Werner et al.*, 2013; *Abarca et al.*, 2013]. According to the United Nations, about 60 percent of world's population lives in coastal areas [*Cosgrove*, 2012], and many aquifers in these areas are saline. Management of aquifer recharge (MAR) is a promising technology, with many operational sites, to help secure water resources [*Dillon*, 2005]. This technology consists in the intentional recharge of water into aquifers, and may have three major benefits: water storage for later use, recharging aquifers subject to falling water levels, and water quality improvements by physical filtration and biodegradation. MAR is also a major technology for the mitigation of seawater intrusion [*Merritt*, 1986; *Simmons et al.*, 2001; *Berens et al.*, 2009], and MAR in these coastal saline aquifers will become necessary as seawater intrusion intensifies and freshwater becomes more scarce [*Simmons*, 2005].

One of the major complications for MAR in brackish-saline aquifers is the occurrence of density-driven flows due to the density difference between injected freshwater and ambient saline aquifer. The freshwater–saltwater interface tilting due to the density contrast leads to early breakthrough of saline groundwater and reduces the recoverable volume of water [*Ward et al.*, 2007; *Van Dam et al.*, 2009; *Zuurbier et al.*, 2014]. Numerical simulators for variable

density flow and transport have been developed, and the effect of density difference on freshwater recovery rate has been investigated [*Voss and Souza*, 1987; *Guo and Langevin*, 2002; *Ward et al.*, 2007; *Bakker*, 2010; *Pool and Carrera*, 2010; *Zuurbier et al.*, 2013]. The application of these forward numerical models at field sites for the design of injection and recovery schemes, however, requires an accurate estimation of groundwater model parameters such as the medium permeability. Aquifers are naturally heterogeneous systems with a wide range of permeability values, and aquifer heterogeneity controls the flow of injected freshwater and its mixing with the residing saline groundwater [*Hess et al.*, 1992; *Simmons et al.*, 2001]. Aquifer heterogeneity has been shown to have a major impact on the fraction of recoverable water in MAR sites, and accurate estimation of aquifer heterogeneity can help maximize the recovery efficiency [*Ward et al.*, 2008; *Izbicki et al.*, 2010; *Pool et al.*, 2015b; *Guo et al.*, 2015]. It is also well known that subsurface heterogeneity can lead to anomalous transport behavior, characterized by early arrival and long tails of subsurface fluid plumes [*Becker and Shapiro*, 2000; *Haggerty et al.*, 2001; *Le Borgne and Gouze*, 2008; *Dentz et al.*, 2015; *Kang et al.*, 2015]. Thus, an accurate characterization of subsurface heterogeneity is essential for site selection and operation of MAR.

Geophysical methods such as electrical imaging and electromagnetic methods have been applied successfully to delineate the freshwater–saline water interface [*Lebbe*, 1999; *Abdalla et al.*, 2010; *Minsley et al.*, 2011; *Maliva*, 2015]. However, inferring hydraulic conductivity information from electrical and electromagnetic signal is challenging due to the uncertainty in the constitutive law [*Slater*, 2007]. The most easily measurable kind of data that is directly sensitive to fluid flow properties is pressure data. Pressure data alone is generally insufficient to accurately image the subsurface under constant-fluid-density groundwater flows, and requires a

dense sampling network combined with multiple pumping tests [*Li et al.*, 2005; *Alcolea et al.*, 2007; *Cardiff et al.*, 2012, 2013] or additional sources of information from either tracer transport or geophysical monitoring [*Woodbury et al.*, 1987; *Pavelic et al.*, 2006; *Fienen et al.*, 2009; *Li et al.*, 2012; *Lee and Kitanidis*, 2014; *Zhang et al.*, 2014; *Kang et al.*, 2016]. In the presence of variable-density flow, however, fluid pressure is coupled to the salinity distribution. Does, then, a density contrast between injected and ambient fluids make pressure data more informative for subsurface characterization? This is the central question that we address in this study.

When there is a salinity difference between the injected and ambient fluids, due to the coupling between the salinity-controlled density-driven flow and the changes in salinity distribution, the pressure data becomes time-dependent. Our key hypothesis here is that the transient pressure data caused by density-dependent flow can provide high quality information for characterizing the subsurface permeability field. The hypothesis is based on the recognition that the concentration-dependent density term couples pressure and transport equations. With the added temporal dynamics, the transient pressure data may provide additional details of the permeability field that steady-state pressure data cannot provide. To test our hypothesis, we perform Bayesian geostatistical inversion for different scenarios of fluid injection, with and without density-driven flow. We also present inversion results for different types of permeability fields and different values of the mixed convection ratio, which determines the relative importance between injection-driven viscous forces and gravitational forces. We show that a variable density makes pressure data more informative, thus enabling more accurate subsurface inversion as the mixed convection ratio increases.

2. Conceptual Background

2.1. Problem Setup

The conceptual model is mainly motivated by the MAR site in South Korea. The site has multiple injection and observation wells and the ambient groundwater has a salinity close to seawater. We study the case where the freshwater is injected simultaneously through a linear arrangement of a number of wells [*Nicot*, 2008; *MacMinn et al.*, 2010; *Szulczewski et al.*, 2012]. While a single well injection forms a radial flow geometry, the injection from a line array of wells will interfere and the flow becomes linear as the radius of the plumes approaches the inter-well spacing.

The synthetic field set up and model input parameters are shown in Figure 1 and Table 1. We inject freshwater into a saline aquifer from the left boundary, simulating a fully penetrating well. There are five observation wells with multilevel groundwater monitoring, which give pressure data at five discrete levels [*Pickens et al.*, 1978; *Foster and D.*, 1989; *Einarson and Cherry*, 2002]. Two different types of "true" log permeability fields are generated using Gaussian and exponential covariance models, and we use pressure data to estimate heterogeneous permeability fields.

2.2. Mixed Convection Ratio

There are three driving forces that control the density-driven groundwater flow in the system: the gravitational force due to the density contrast, the external viscous force due to the injection, and the dispersive force due to the concentration gradient. The interplay between these three driving forces control the flow dynamics and the relative importance between these three forces can be quantified with dimensionless numbers. The Rayleigh number compares gravitational force to dispersive force, $Ra = \frac{\text{Gravitation}}{\text{Dispersion}}$, the Péclet number compares injection force to

dispersive force $Pe = \frac{\text{External}}{\text{Dispersion}}$, and the mixed convection ratio compares gravitational force to external force, $M = \frac{\text{Gravitation}}{\text{External}}$ [*Holzbecher*, 2000; *Ward et al.*, 2007].

The mixed convection ratio is shown to control the flow dynamics in saline aquifers and, as a result, the freshwater recovery efficiency [*Massmann et al.*, 2006; *Ward et al.*, 2007]. The mixed convection ratio can also be understood as the ratio between forced convection and free convection, where forced convection is the advection due to pumping, and free convection is the advection caused by the density difference between injected freshwater and ambient saline water. Therefore, we define the mixed convection ratio as

$$M = \frac{Ra}{Pe} = \frac{v_{\text{free}}}{v_{\text{forced}}} = \frac{k_m \Delta\rho g B}{\mu Q} \tag{1}$$

where k_m [L^2] is the mean permeability, $\Delta\rho$ [ML^{-3}] is the density difference between injected freshwater and saline groundwater, g [LT^{-2}] is the gravitational constant, B [L] is the aquifer depth in z direction, μ [$ML^{-1}T^{-1}$] is the dynamic viscosity of the fluid, and Q [$L^3T^{-1}L^{-1}$] is the injection rate into a cross section with height B and unit thickness. The specific units of the variables can be found in Table 1. The characteristic velocity associated with forced convection is defined as, $v_{\text{forced}} = \frac{Q}{B\phi}$, and with free convection is defined as, $v_{\text{free}} = \frac{k_m \Delta\rho g}{\mu\phi}$ where ϕ is the porosity. Since advection arises from two different mechanisms, we call this the mixed convection ratio. Density differences dominate the flow in the system when $M \gg 1$, and fluid injection dominates the flow when $M \ll 1$. The case $M = 0$ corresponds to the situation in which there is no density contrast, which is equivalent to injecting a matched-density fluid with a passive tracer. We study the value of transient pressure data at different mixed convective regimes.

3. Numerical Simulation of Variable Density Groundwater Flow and Transport

The density-driven flow and transport of two miscible fluids in a groundwater system can be described by the so-called Boussinesq approximation when $\frac{Ra}{\epsilon} \gg 1$ where ϵ is the density difference ratio, $\epsilon = \frac{\rho_{\max} - \rho_0}{\rho_0}$ [*Landman and Schotting*, 2007]. The Boussinesq approximation is valid for realistic scenarios in saline confined MAR sites. The governing equations for variable-density flow under the Boussinesq approximation are [*Riaz et al.*, 2006; *Landman and Schotting*, 2007; *Elenius et al.*, 2012; *Hidalgo et al.*, 2012; *Szulczewski and Juanes*, 2013]:

$$\nabla \cdot \mathbf{u} = 0 \tag{2a}$$

$$\mathbf{u} = -\frac{\mathbf{k}}{\mu}(\nabla p - \rho(c) g \mathbf{z}) \tag{2b}$$

$$\phi \frac{\partial c}{\partial t} + \nabla \cdot (\mathbf{u} c - \phi \mathbf{D}_{\text{eff}} \nabla c) = 0 \tag{2c}$$

The governing equations consist of the mass conservation equation, Darcy's law, and the advection–dispersion equation, where $\mathbf{k}$ is the permeability field, ρ is the fluid density, and $\mathbf{D}_{\text{eff}}$ is the effective dispersion coefficient. We adopt the Scheidegger–Bear dispersion model: $\phi D^{ij}_{\text{eff}} = (\phi D_0 + \beta_T |\mathbf{u}|)\delta_{ij} + (\beta_L - \beta_T)\frac{u_i u_j}{|\mathbf{u}|}$, where D_0 is the molecular diffusivity, $|\mathbf{u}|$ is the magnitude of the Darcy velocity, β_{L} is the longitudinal dispersivity, and β_{T} is the transverse dispersivity. Density is given as a linear function of concentration, $\rho = \rho_0 + \frac{\partial \rho}{\partial c}(c - c_0)$ where $\frac{\partial \rho}{\partial c} = 700$ [kg/m^3] and ρ_0 is the density of freshwater [*Voss and Souza*, 1987]. c is the concentration of solute as a mass fraction of dissolved salt in water (mass of dissolved salt per unit mass of fluid), and $c = 0$ for injected freshwater and $c > 0$ for saline groundwater. The aquifer is initially fully saturated with saline groundwater and we start to inject freshwater at $t = 0$.

The boundary conditions are

$$\mathbf{u} \cdot \mathbf{n}(x = 0, z, t) = v_{\text{forced}} \tag{3a}$$

$$\mathbf{u} \cdot \mathbf{n}(x, z = 0 \text{ or } B, t) = 0 \tag{3b}$$

$$p(x = L, z, t) = \rho_{\text{sea}} g z \tag{3c}$$

where $\mathbf{n}$ is the outward unit normal to the boundary. We inject with a constant flow rate from the left boundary and assign a hydrostatic pressure boundary condition at the right boundary [*Voss and Souza*, 1987]. The domain size is 250 m $\times$ 50 m. We assign no-flow boundary conditions at the top and bottom boundaries to describe a confined aquifer. We inject freshwater using a fully screened well and measure pressure values at 25 data sampling points. We employ a high-resolution, high-order forward numerical simulator to solve the full, two-dimensional system of governing equations. For all simulations, the model domain is discretized into square elements with $\Delta x = \Delta z = 0.5$ m. We solve the pressure field using the finite volume method with the two-point flux approximation (TPFA), and solve for the concentration field using 6th order finite compact difference [*Lele*, 1992]. We integrate in time using an explicit 4th order Runge-Kutta time-stepping scheme [*Jha et al.*, 2011; *Nicolaides et al.*, 2015]. The high-resolution, high-order model allows us to accurately capture density-driven flow and dispersive mixing under forced injection. The detailed model input parameters are shown in Table 1.

In this study, we investigate the effects of density-driven flow on permeability characterization for different values of mixed convection ratios and different types of permeability fields. To study the effects of the mixed convection ratio on the inversion results, we study three different mixed convection ratios, $M = 0, 0.21$ and 0.42. To avoid effects from other parameters, we vary the mixed convection ratio only by changing the density difference between injected freshwater and ambient groundwater. We fix the injection rate to avoid changing Péclet number. $M = 0$

corresponds to the case when there is no density contrast between injected water and residing groundwater, which results in steady-state groundwater flow. $M = 0.21$ and $M = 0.42$ correspond to residence groundwater concentrations of $c = 0.0175$ [kg/kg] and $c = 0.035$ [kg/kg], respectively. The freshwater injection duration is 20 days. To confirm the generality of our inversion results, we study five different log-normal permeability fields for each covariance model (Gaussian and exponential).

4. Inversion with the Principal Component Geostatistical Approach (PCGA)

To infer the permeability distribution from the pressure data, we consider the following observation equation:

$$\mathbf{p} = \mathbf{h}(\mathbf{s}) + \mathbf{v} \tag{4}$$

where $\mathbf{p}$ is the observed pressure data vector at monitoring wells, $\mathbf{h}$ is a forward model described in Equation 2, $\mathbf{s}$ is the unknown lognormal permeability field (e.g $\mathbf{s} = \log_{10} k$), and $\mathbf{v}$ is the error in the observation data $\mathbf{y}$ as well as the simulation model $\mathbf{h}$, usually modeled as Gaussian. To estimate the unknown $\mathbf{s}$ from the data and the forward model, we employ the Bayesian geostatistical inverse approach [*Kitanidis*, 1995]. The prior probability density function (pdf) of $\mathbf{s}$ is assumed to be Gaussian with an unknown mean and a prior covariance matrix $\mathbf{Q}$. Then, the posterior pdf of $\mathbf{s}$ is computed through Bayes' theorem, and the maximum a posteriori (MAP) estimate or most likely value of $\mathbf{s}$ is obtained by maximizing the posterior pdf (typically minimizing the negative logarithm of the posterior pdf). The inverse problem becomes a nonlinear optimization problem that is commonly solved using an iterative Gauss–Newton method. However, the geostatistical approach becomes computationally challenging for large-scale inversions because it requires computation of the derivative of the forward model, i.e., the Jacobian matrix

$\mathbf{H}$ at a current estimate $\tilde{\mathbf{s}}$,

$$H_{ij} = \frac{\partial h_i}{\partial s_j}|_{\mathbf{s}=\tilde{\mathbf{s}}} \tag{5}$$

which has a computational cost proportional to the number of observations, even in the efficient adjoint-state method. Furthermore, the adjoint-state method needs intrusive changes in the forward model code, which can be an added practical challenge for coupled multi-physics models like the one here.

To circumvent those computational requirements and code development issues, we use PCGA, which expedites the geostatistical inversion by avoiding the direct evaluation of the Jacobian matrix $\mathbf{H}$ using a low-rank approximation of the prior covariance matrix $\mathbf{Q}$ and a finite difference calculation of sensitivities based on the forward model. This can be made possible due to the fact that the geostatistical approach requires Jacobian-covariance products such as $\mathbf{HQ}$, not the Jacobian itself. Assume that the covariance matrix $\mathbf{Q}$ is approximated as

$$\mathbf{Q} = \mathbf{Q}_\kappa = \sum_{i=1}^{\kappa} \zeta_i \zeta_i^\top \tag{6}$$

where $\mathbf{Q}_\kappa$ is a rank-κ approximation of $\mathbf{Q}$ and ζ_i is i-th eigenvector multiplied by square root of i-th eigenvalue of $\mathbf{Q}$. A fast and accurate method to obtain Equation 6 for large-scale covariance matrices is explained in *Lee and Kitanidis* [2014]. Then, the Jacobian-covariance product $\mathbf{HQ}$ can be approximated:

$$\mathbf{HQ} = \mathbf{H}\left(\sum_{i=1}^{\kappa} \zeta\zeta^\top\right) = \sum_{i=1}^{\kappa} \left(\mathbf{H}\zeta_i\right)\zeta_i^\top \tag{7}$$

where $\mathbf{H}\zeta_i$ is computed as

$$\mathbf{H}\zeta_i \approx \frac{\mathbf{h}(\mathbf{s}+\delta\zeta_i) - \mathbf{h}(\mathbf{s})}{\delta} \tag{8}$$

where δ is the finite difference perturbation size. A detailed explanation on the optimal choice of κ and δ can be found in *Lee and Kitanidis* [2014]; *Lee et al.* [2016]. Thus, only about

223 "κ" forward simulation evaluations are needed to obtain the inverse solution at each iteration.
224 Previous numerical experiments [*Lee and Kitanidis*, 2014; *Lee et al.*, 2015; *Fakhreddine et al.*,
225 2016] have shown that $\kappa \sim \mathcal{O}(100)$ and a few hundred simulation runs in total are needed
226 without any intrusive changes in the simulation model code to arrive at inverse solutions of the
227 same quality as those obtained from the geostatistical approach.

228 In this work, PCGA is used to estimate permeability fields from synthetic pressure data mea-
229 sure at the 5×5 sampling network shown in Figure 1. A Gaussian error with zero mean and
230 standard deviation of 300 $\mathrm{N/m^2}$ was added to the simulated pressure measurements. This error
231 corresponds to 50% of the maximum pressure change during the fresh injection. The data were
232 recorded every five minutes for 20 days and the number of pressure measurements amounts to
233 144,000 in total for the saline aquifer injection cases (i.e., $M = 0.21$ and 0.42). All inversion
234 cases were run on a Linux workstation equipped with 36 Intel core 3.1 GHz processors and
235 128 GB RAM, and κ was chosen to be 324 (36×9) to take advantage of running the forward
236 solvers on 36 cores simultaneously. One entire inversion run with a density-driven pressure data
237 set took 9 hours on average, and all the tests converged within 6 iterations. All the inversion runs
238 used an exponential covariance function for the prior and corresponding structural parameters
239 for the prior covariance $\mathbf{Q}$ and the error $\mathbf{R}$ were determined using the cR/Q2 criteria [*Kitanidis*,
240 1991].

5. Results and Discussion

241 The mixed convection ratio has a significant impact on plume spreading and fluid pressure
242 distribution (Figure 2). When there is no density contrast between injected and defending fluids,
243 the pressure field is steady (constant in time). For $M = 0.21$ and $M = 0.42$, we clearly observe
244 the change in pressure over time due to the density-driven flow. Note that the relative pressure

change for $M = 0.42$ is larger than for $M = 0.21$. This is because the free convection component that causes the pressure change is larger for larger mixed convection ratio. Moreover, the pressure change exhibits a nontrivial behavior as the change starts before the injected fluid reaches a sampling point. This shows that the change in freshwater–saline groundwater interface influences the pressure distribution globally. The pressure data alone in density invariant flow is known to capture large-scale features of permeability fields and the joint inversion with concentration data is necessary to improve the imaging quality of small scale features [*Cirpka and Kitanidis*, 2000; *Lee and Kitanidis*, 2014]. Now the key question is whether the sampling of this transient pressure field in variable-density flow can better inform about the subsurface permeability structure. To answer this question, we perform permeability-field inversion in the synthetic MAR site shown in Figure 1 using pressure data.

We present the inversion results obtained by applying PCGA to different mixed convection ratios and different types of permeability field. The inversion results for a permeability field with Gaussian covariance function is shown in Figure 3. It is visually clear that the increase in density contrast leads to improved characterization results, along with reduced uncertainty. Figure 4 shows the crossplot between observed and simulated pressures for three inversion scenarios with different mixed convection ratios. When there is no density contrast, we obtain a smoothed permeability estimate at best from the steady-state pressure data due to the diffusive nature of pressure distribution. Improvements in the characterization result would typically require complementing the pressure data with other types of the data such as concentration, and performing joint inversion [e.g., *Lee and Kitanidis*, 2014]. For cases with density contrast between injected and ambient fluids, the pressure field is no longer steady but, instead, changes with time due to density-driven flow. The change in system dynamics increases the number of

pressure measurements that can be utilized in the inversion, and the transient pressure measurement implicitly has concentration information through coupled flow and transport equations in Equation 2. It has been shown that joint inversion with pressure and concentration data can improve the inversion results dramatically by capturing both large-scale features from pressure and small-scale details from concentration [e.g., *Cirpka and Kitanidis*, 2000; *Lee and Kitanidis*, 2014]. *Pool et al.* [2015a] also showed in a field-based study that adding concentration data into the inversion framework lead to better match the measured concentration data. The current work is similar to the joint inversion in that the transient pressure data implicitly contains transport information.

As shown in Figure 5, the inversion results for the permeability fields with exponential covariance function show very similar results to those obtained with Gaussian permeability fields. We obtain a smoothed permeability estimate without any local heterogeneity information from the steady-state pressure data. The increase in the density contrast significantly improves the inversion results. Figure 6 shows the crossplot between simulated and observed pressure indicating that the estimated permeability fields can accurately capture observed pressure data.

To confirm the generality of our findings, we performed the inversion for five different realizations for both Gaussian and exponential permeability fields. We then rigorously assess the performance of permeability estimation using three different measures. We first compute the inversion performance as a function of mixed convection ratio by calculating the residual sum of squares between the true and estimated permeability fields (RSS_k) for five realizations. RSS_k is defined as, $\text{RSS}_k = \sum_i (s_i - \tilde{s_i})$, where s_i is the true permeability value of the ith element and $\tilde{s_i}$ is an estimated permeability value of the ith element. Figure 7(a) clearly shows that the increase in density contrast improves the inversion result. Figure 7(b) shows that, as was the

case for the Gaussian covariance function, a higher density contrast between background saline water and injected freshwater improves the characterization of the permeability field also for the exponential covariance function.

As a second measure, we perform the transport predictability tests with passive tracers; that is, with no density contrast between injected and ambient fluids. This permits comparing transport predictions of the inverted permeability fields obtained at different mixed convection ratios, since transport will be governed by permeability heterogeneity alone. To confirm the generality of transport predictability, we calculate the residual sum of squares (RSS) of breakthrough curves measured at the 5×5 data sampling network. RSS for each breakthrough curve is defined as $\text{RSS}_j = \sum_i (c_i^j - \tilde{c}_i^j)$, where c_i^j is the *true* concentration value of the ith measurement of the jth breakthrough curve and $\tilde{c}_i^j$ is an *estimated* concentration value of the ith measurement of the jth breakthrough curve. We measure 25 RSS measurements for each realization and a total of 125 RSS values for each mixed convection ratio. As shown in Fig. 8, transport predictability improves with mixed convection ratio.

The quality of the estimated permeability field is also assessed by a mapping accuracy evaluation. Mapping accuracy is defined as the fraction of the permeability field where the difference between the true and estimated log permeability values is less than a certain threshold [*Yoon and McKenna*, 2012; *Lee et al.*, 2016]. In this study, we set the threshold as 15% of the difference between the maximum and minimum values of the true log-permeability field. A higher mapping accuracy indicates higher fractions of accurately estimated permeability. Fig. 9 shows that the mapping accuracy increases with the mixed convection ratio, and the increasing trend is clearer for Gaussian permeability field. For both Gaussian and exponential permeability fields,

all three measures show that the inversion accuracy increases as the density contrast increases. This confirms that our finding applies to permeability fields with different statistical properties.

Finally, we have performed additional inversion tests at higher heterogeneity, $\sigma^2_{\ln k} = 0.5$. As shown in Fig. 10 and Fig. 11, we clearly observe that the existence of a density contrast still improves the inversion performance for higher heterogeneity, so the main point of our paper stands. However, a more detailed study is necessary to study the effects of density contrast on saline aquifer characterization at higher levels of heterogeneity.

6. Conclusions

We have shown that the transient pressure data in variable density flow provides robust information for effective subsurface imaging. In density-driven flow, the pressure data becomes time-dependent since density is a function of salt concentration. The transient pressure measurement implicitly contains concentration information through the coupled flow and transport equations, so that inversion with transient pressure alone produces inversion results that are similar to those from joint inversion.

The mixed convection ratio is the central parameter determining the accuracy of the inversion: inversion accuracy increases as density contrast increases. In real field applications, the mixed convection ratio can be engineered by varying the injection rate. However, change in the injection rate will also change the Péclet number which can have nontrivial effects on inversion. These combined effects will be the topic of a future study. In reality, additional challenges may arise in association with 3D flow. A relatively dense 3D array of data sampling networks may be required to characterize the 3D permeability field. An extension of this study to 3D heterogeneous aquifers with a realistic monitoring system will be necessary to address the challenges of applying our findings to field sites.

Our work suggests new opportunities to effectively image subsurface heterogeneity utilizing variable density flow. We anticipate that from a small number of pumping tests in which transient multisample pressure data is collected would be sufficient to accurately estimate the permeability field, thus reducing the cost of site characterization. Tracer concentration and electrical resistivity data are also commonly used data types for saline aquifer characterization. The effects of the density-driven flow on the value of different data types will be the focus of a future study. This will help field practitioners to choose the best combination of data sets for improved saline aquifer characterization. Density-driven flow occurs at MAR, sea water intrusion and geologic carbon dioxide sequestration sites, and these applications can potentially benefit from this work.

During MAR in brackish-saline aquifers, the density contrast between injected and residing fluids can be a major challenge for maximizing recovery efficiency. While a small amount of salinity in the recovered water can be detrimental to MAR operations, in this study we show that the density contrast can be actually utilized for efficient heterogeneity characterization. The density effect in saline aquifers can reduce recovery efficiency, but on the other hand can play an effective role in subsurface characterization. With the accurately characterized heterogeneous permeability field obtained from freshwater injection experiments, the recovery efficiency can be improved by optimizing injection-withdrawal locations and operational strategies.

Acknowledgments. Peter K. Kang and Seunghak Lee acknowledge Ministry of Land, Infrastructure and Transport, Korea (16AWMP-B066761-04), the Future Research Program (2E27030) funded by the Korea Institute of Science and Technology (KIST), and the National Research Foundation of Korea Grant funded by the Korean Government (MSIP) (2016,

University-Institute cooperation program) for their support. Jonghyun Lee and Peter K. Kitanidis acknowledge the support of the National Science Foundation through its ReNUWIt Engineering Research Center (www.renuwit.org; NSF EEC-1028968). Xiaojing Fu and Ruben Juanes acknowledge support from the U.S. Department of Energy through a DOE Mathematical Multifaceted Integrated Capability Center (grant DE-SC0009286), and from the MIT International Science and Technology Initiatives (MISTI) through a Global Seed Funds award. The data to reproduce the work can be obtained from the first author: Peter K. Kang (pkkang@kist.re.kr).

References

Abarca, E., H. Karam, H. F. Hemond, and C. F. Harvey (2013), Transient groundwater dynamics in a coastal aquifer: The effects of tides, the lunar cycle, and the beach profile, *Water Resour. Res.*, *49*(5), 2473–2488.

Abdalla, O. A. E., M. Ali, K. Al-Higgi, H. Al-Zidi, I. El-Hussain, and S. Al-Hinai (2010), Rate of seawater intrusion estimated by geophysical methods in an arid area: Al khabourah, oman, *Hydrogeol. J.*, *18*(6), 1437–1445.

Aeschbach-Hertig, W., and T. Gleeson (2012), Regional strategies for the accelerating global problem of groundwater depletion, *Nat. Geosci.*, *5*(12), 853–861.

Alcolea, A., E. Castro, M. Barbieri, J. Carrera, and S. Bea (2007), Inverse modeling of coastal aquifers using tidal response and hydraulic tests, *Ground Water*, *45*(6), 711–722.

Bakker, M. (2010), Radial dupuit interface flow to assess the aquifer storage and recovery potential of saltwater aquifers, *Hydrogeol. J.*, *18*(1), 107–115.

Becker, M. W., and A. M. Shapiro (2000), Tracer transport in fractured crystalline rock: Evidence of nondiffusive breakthrough tailing, *Water Resour. Res.*, *36*(7), 1677–1686.

379 Berens, V., M. G. White, and N. J. Souter (2009), Injection of fresh river water into a saline
380 floodplain aquifer in an attempt to improve the condition of river red gum (eucalyptus camal-
381 dulensis dehnh.), *Hydrol. Process.*, *23*(24), 3464–3473.

382 Cardiff, M., W. Barrash, and P. K. Kitanidis (2012), A field proof-of-concept of aquifer imaging
383 using 3-d transient hydraulic tomography with modular, temporarily-emplaced equipment,
384 *Water Resour. Res.*, *48*(5), doi:10.1029/2011WR011704.

385 Cardiff, M., T. Bakhos, P. K. Kitanidis, and W. Barrash (2013), Aquifer heterogeneity charac-
386 terization with oscillatory pumping: Sensitivity analysis and imaging potential, *Water Resour.*
387 *Res.*, *49*(9), 5395–5410.

388 Cirpka, O. A., and P. K. Kitanidis (2000), Sensitivity of temporal moments calculated by the
389 adjoint-state method and joint inversing of head and tracer data, *Adv. Water Resour.*, *24*(1),
390 89–103.

391 Cosgrove, W. J. (2012), *The United Nations World Water Development Report–N 4–The Dy-*
392 *namics of Global Water Futures: Driving Forces 2011–2050*, vol. 2, UNESCO.

393 Dentz, M., P. K. Kang, and T. Le Borgne (2015), Continuous time random walks for non-local
394 radial solute transport, *Adv. Water Resour.*, *82*, 16–26.

395 Dillon, P. (2005), Future management of aquifer recharge, *Hydrogeol. J.*, *13*(1), 313–316.

396 Einarson, M. D., and J. A. Cherry (2002), A new multilevel ground water monitoring system
397 using multichannel tubing, *Ground Water Monit. R.*, *22*(4), 52–65.

398 Elenius, M. T., J. M. Nordbotten, and H. Kalisch (2012), Effects of a capillary transition zone
399 on the stability of a diffusive boundary layer, *IMA J. of Appl. Math.*, *77*(6), 771–787.

400 Fakhreddine, S., J. Lee, P. K. Kitanidis, S. Fendorf, and M. Rolle (2016), Imaging geochemical
401 heterogeneities using inverse reactive transport modeling: An example relevant for character-

izing arsenic mobilization and distribution advances in water resources, *Adv. Water Resour.*, *88*, 186–197.

Fienen, M., R. Hunt, D. Krabbenhoft, and T. Clemo (2009), Obtaining parsimonious hydraulic conductivity fields using head and transport observations: A bayesian geostatistical parameter estimation approach, *Water Resour. Res.*, *45*(8), doi:10.1029/2008WR007431.

Foster, S., and C. D. (1989), Groundwater quality monitoring: an appraisal of practices and costs, in *Groundwater quality monitoring: an appraisal of practices and costs*, CEPIS.

Gleeson, T., Y. Wada, M. F. P. Bierkens, and L. P. H. van Beek (2012), Water balance of global aquifers revealed by groundwater footprint, *Nature*, *488*(7410), 197–200.

Guo, W., and C. D. Langevin (2002), User's guide to SEAWAT; a computer program for simulation of three-dimensional variable-density ground-water flow, *Tech. Rep. No. 06-A7*.

Guo, W. X., K. Coulibaly, and R. G. Maliva (2015), Simulated effects of aquifer heterogeneity on ASR system performance, *Environ. Earth Sci.*, *73*(12), 7803–7809.

Haggerty, R., S. W. Fleming, L. C. Meigs, and S. A. McKenna (2001), Tracer tests in a fractured dolomite 2. Analysis of mass transfer in single-well injection-withdrawal tests, *Water Resour. Res.*, *37*, 1129–1142.

Hess, K. M., S. H. Wolf, and M. A. Celia (1992), Large-scale natural gradient tracer test in sand and gravel, cape cod, massachusetts 3. hydraulic conductivity variability and calculated macrodispersivities, *Water Resour. Res.*, *28*(8), 2011–2027.

Hidalgo, J. J., J. Fe, L. Cueto-Felgueroso, and R. Juanes (2012), Scaling of convective mixing in porous media, *Phys. Rev. Lett.*, *109*, 264,503.

Holzbecher, E. (2000), Comment on 'Mixed convection processes below a saline disposal basin' by Simmons, CT, Narayan KA, 1997. Journal of Hydrology 194, 263–285, *J. Hydrol.*, *229*(3),

425 290–295.

426 Izbicki, J. A., et al. (2010), Aquifer storage recovery (ASR) of chlorinated municipal drinking
427 water in a confined aquifer, *Appl. Geochem.*, *25*(8), 1133–1152.

428 Jha, B., L. Cueto-Felgueroso, and R. Juanes (2011), Quantifying mixing in viscously unstable
429 porous media flows, *Phys. Rev. E*, *84*(6), 066,312.

430 Kang, P. K., T. Le Borgne, M. Dentz, O. Bour, and R. Juanes (2015), Impact of velocity corre-
431 lation and distribution on transport in fractured media: Field evidence and theoretical model,
432 *Water Resour. Res.*, *51*(2), 940–959, doi:10.1002/2014WR015,799.

433 Kang, P. K., Y. Zheng, X. Fang, R. Wojcik, D. McLaughlin, S. Brown, M. C. Fehler,
434 D. R. Burns, and R. Juanes (2016), Sequential approach to joint flow–seismic inversion
435 for improved characterization of fractured media, *Water Resour. Res.*, *52*(2), 903–919,
436 doi:10.1002/2015WR017,412.

437 Kitanidis, P. K. (1991), Orthonormal residuals in geostatistics - model criticism and parameter-
438 estimation, *Math. Geol.*, *23*(5), 741–758.

439 Kitanidis, P. K. (1995), Quasi-linear geostatistical theory for inversing, *Water Resour. Res.*,
440 *31*(10), 2411–2419.

441 Landman, A. J., and R. J. Schotting (2007), Heat and brine transport in porous media: the
442 oberbeck-boussinesq approximation revisited, *Transport Porous Med.*, *70*(3), 355–373.

443 Le Borgne, T., and P. Gouze (2008), Non-Fickian dispersion in porous media: 2. Model valida-
444 tion from measurements at different scales, *Water Resour. Res.*, *44*, W06,427.

445 Lebbe, L. (1999), Parameter identification in fresh-saltwater flow based on borehole resistivities
446 and freshwater head data, *Adv. Water Resour.*, *22*(8), 791–806.

Lee, J., and P. K. Kitanidis (2014), Large-scale hydraulic tomography and joint inversion of head and tracer data using the Principal Component Geostatistical Approach (PCGA), *Water Resour. Res.*, *50*(7), 5410–5427.

Lee, J., A. Kokkinaki, Y. Li, and P. K. Kitandis (2015), Fast large-scale inversion for deep aquifer characterization, in *TOUGH2 Symposium*, Lawrence Berkeley National Laboratory, Berkeley, California.

Lee, J., H. Yoon, P. K. Kitanidis, C. J. Werth, and A. J. Valocchi (2016), Scalable subsurface inverse modeling of huge data sets with an application to tracer concentration breakthrough data from magnetic resonance imaging, *Water Resour. Res.*, *52*(7), 5213–5231, doi: 10.1002/2015WR018483.

Lele, S. K. (1992), Compact finite difference schemes with spectral-like resolution, *J. Comput. Phys.*, *103*(1), 16–42.

Li, L., H. Zhou, J. J. Gómez-Hernández, and H. J. Hendricks Franssen (2012), Jointly mapping hydraulic conductivity and porosity by assimilating concentration data via ensemble kalman filter, *J. Hydrol.*, *428*, 152–169.

Li, W., W. Nowak, and O. A. Cirpka (2005), Geostatistical inverse modeling of transient pumping tests using temporal moments of drawdown, *Water Resour. Res.*, *41*(8), doi: 10.1029/2004WR003874.

MacMinn, C. W., M. L. Szulczewski, and R. Juanes (2010), CO_2 migration in saline aquifers. Part 1. Capillary trapping under slope and groundwater flow, *J. Fluid Mech.*, *662*, 329–351.

Maliva, R. G. (2015), Managed aquifer recharge: state-of-the-art and opportunities, *Water Sci. Technol.*, *15*(3), 578–588.

Massmann, G., C. Simmons, A. Love, J. Ward, and J. James-Smith (2006), On variable density surface water–groundwater interaction: a theoretical analysis of mixed convection in a stably-stratified fresh surface water–saline groundwater discharge zone, *J. Hydrol.*, *329*(3), 390–402.

Merritt, M. L. (1986), Recovering fresh water stored in saline limestone aquifers, *Ground Water*, *24*(4), 516–529.

Minsley, B. J., J. Ajo-Franklin, A. Mukhopadhyay, and F. D. Morgan (2011), Hydrogeophysical methods for analyzing aquifer storage and recovery systems, *Ground Water*, *49*(2), 250–269.

Nicolaides, C., B. Jha, L. Cueto-Felgueroso, and R. Juanes (2015), Impact of viscous fingering and permeability heterogeneity on fluid mixing in porous media, *Water Resour. Res.*, *51*(4), 2634–2647.

Nicot, J.-P. (2008), Evaluation of large-scale CO_2 storage on fresh-water sections of aquifers: An example from the Texas gulf coast basin, *Intl J. Greenh. Gas Control*, *2*(4), 582–593.

Pavelic, P., P. J. Dillon, and C. T. Simmons (2006), Multiscale characterization of a heterogeneous aquifer using an ASR operation, *Ground Water*, *44*(2), 155–164.

Pickens, J. F., J. A. Cherry, G. E. Grisak, W. F. Merritt, and B. A. Risto (1978), Multilevel device for groundwater sampling and piezometric monitoring, *Ground Water*, *16*(5), 322–327.

Pool, M., and J. Carrera (2010), Dynamics of negative hydraulic barriers to prevent seawater intrusion, *Hydrogeol. J.*, *18*(1), 95–105.

Pool, M., J. Carrera, A. Alcolea, and E. M. Bocanegra (2015a), A comparison of deterministic and stochastic approaches for regional scale inverse modeling on the mar del plata aquifer, *J. Hydrol.*, *531*, 214–229.

Pool, M., V. E. A. Post, and C. T. Simmons (2015b), Effects of tidal fluctuations and spatial heterogeneity on mixing and spreading in spatially heterogeneous coastal aquifers, *Water*

Resour. Res., *51*(3), 1570–1585.

Riaz, A., M. Hesse, H. A. Tchelepi, and F. M. Orr (2006), Onset of convection in a gravitationally unstable diffusive boundary layer in porous media, *J. Fluid Mech.*, *548*, 87–111.

Rijsberman, F. R. (2006), Water scarcity: fact or fiction?, *Agric. Water Manage.*, *80*(1), 5–22.

Simmons, C. T. (2005), Variable density groundwater flow: From current challenges to future possibilities, *Hydrogeol. J.*, *13*(1), 116–119.

Simmons, C. T., T. R. Fenstemaker, and J. M. Sharp (2001), Variable-density groundwater flow and solute transport in heterogeneous porous media: approaches, resolutions and future challenges, *J. Contaminant Hydrol.*, *52*(1), 245–275.

Slater, L. (2007), Near surface electrical characterization of hydraulic conductivity: From petrophysical properties to aquifer geometries–A review, *Surv. Geophys.*, *28*(2-3), 169–197.

Szulczewski, M. L., and R. Juanes (2013), The evolution of miscible gravity currents in horizontal porous layers, *J. Fluid Mech.*, *719*, 82–96.

Szulczewski, M. L., C. W. MacMinn, H. J. Herzog, and R. Juanes (2012), Lifetime of carbon capture and storage as a climate-change mitigation technology, *Proc. Natl. Acad. Sci. USA*, *109*(14), 5185–5189.

Van Dam, R. L., C. T. Simmons, D. W. Hyndman, and W. W. Wood (2009), Natural free convection in porous media: First field documentation in groundwater, *Geophys. Res. Lett.*, *36*(11), doi:10.1029/2008GL036906.

Vörösmarty, C. J., P. Green, J. Salisbury, and R. B. Lammers (2000), Global water resources: vulnerability from climate change and population growth, *Science*, *289*(5477), 284–288.

Voss, C. I., and W. R. Souza (1987), Variable density flow and solute transport simulation of regional aquifers containing a narrow freshwater-saltwater transition zone, *Water Resour.*

Res., *23*(10), 1851–1866.

Ward, J. D., C. T. Simmons, and P. J. Dillon (2007), A theoretical analysis of mixed convection in aquifer storage and recovery: How important are density effects?, *J. Hydrol.*, *343*(3), 169–186.

Ward, J. D., C. T. Simmons, and P. J. Dillon (2008), Variable-density modelling of multiple-cycle aquifer storage and recovery (ASR): Importance of anisotropy and layered heterogeneity in brackish aquifers, *J. Hydrol.*, *356*(1-2), 93–105.

Werner, A. D., M. Bakker, V. E. A. Post, A. Vandenbohede, C. Lu, B. Ataie-Ashtiani, C. T. Simmons, and D. A. Barry (2013), Seawater intrusion processes, investigation and management: recent advances and future challenges, *Adv. Water. Resour.*, *51*, 3–26.

Woodbury, A. D., L. Smith, and W. S. Dunbar (1987), Simultaneous inversion of hydrogeologic and thermal data: 1. Theory and application using hydraulic head data, *Water Resour. Res.*, *23*(8), 1586–1606.

Yoon, H., and S. A. McKenna (2012), Highly parameterized inverse estimation of hydraulic conductivity and porosity in a three-dimensional, heterogeneous transport experiment, *Water Resour. Res.*, *48*(10), doi:10.1029/2012WR012149.

Zhang, Z. S., B. Jafarpour, and L. L. Li (2014), Inference of permeability heterogeneity from joint inversion of transient flow and temperature data, *Water Resour. Res.*, *50*(6), 4710–4725.

Zuurbier, K. G., M. Bakker, W. J. Zaadnoordijk, and P. J. Stuyfzand (2013), Identification of potential sites for aquifer storage and recovery (ASR) in coastal areas using ASR performance estimation methods, *Hydrogeol. J.*, *21*(6), 1373–1383.

Zuurbier, K. G., W. J. Zaadnoordijk, and P. J. Stuyfzand (2014), How multiple partially penetrating wells improve the freshwater recovery of coastal aquifer storage and recovery (ASR)

538 systems: A field and modeling study, *J. Hydrol.*, *509*, 430–441.

Figure 1. (a) Conceptual 2D model of a saline MAR site. The colorbar indicates the concentration of the ambient fluid. Red asterisks indicate the 5×5 data sampling network, and the green dashed line indicates the area of interest to be characterized. We impose a constant-flux boundary condition at the injection well and a hydrostatic boundary condition at the right boundary. The aquifer is initially saturated with saline water and we inject freshwater from the left boundary. We impose a nondispersive mass flux boundary condition at the right boundary. (b) Example of true permeability field with Gaussian covariance function. (c) Example of true permeability field with exponential covariance function.

Table 1. Model input parameters

Parameter	**Symbol**	**Value**	**Unit**
Aquifer Length	L	250	[m]
Aquifer depth	B	50	[m]
Effective porosity	ϕ	0.3	[-]
Permeability field type		Gaussian[a], exponential[b]	
Mean permeability	k	10^{-10}	[m^2]
Fluid dynamic viscosity	μ	10^{-3}	[kg/m/s]
Freshwater density	ρ_0	10^3	[kg/m^3]
Variance of $\ln k$	σ^2	$0.25, 0.5$	
Longitudinal dispersivity	β_{L}	1	[m]
Transverse dispersivity	β_{T}	$0.1\beta_{\mathrm{L}}$	[m]
Molecular diffusivity	D_0	10^{-9}	[m^2/s]
Pumping rate	Q	300	[m^3/day/m]
Mixed convection ratio	M	0, 0.21, 0.42	[-]
Injected solute concentration	c_{in}	0	[kg/kg]
Ambient solute concentration	c_0	0, 0.0175, 0.035	[kg/kg]
Number of unknown k values	$n_{\ln k}$	50,000	[-]
Number of measurements	n_{obs}	25 (steady-state), 144,000 (transient)	[-]
Measurement error	σ_{obs}	300	[N/m^2]

[a] covariance kernel $\sigma^2 \exp(-r^2)$, where $r = \sqrt{\left(\frac{x}{l_x}\right)^2 + \left(\frac{z}{l_z}\right)^2}$ with scale parameter $l_x = 30$ m and $l_z = 5$ m

[b] covariance kernel $\sigma^2 \exp(-|r|)$, where $r = \sqrt{\left(\frac{x}{l_x}\right)^2 + \left(\frac{z}{l_z}\right)^2}$ with scale parameter $l_x = 50$ m and $l_y = 5$ m

Figure 2. Forward-model simulation results at four different times, $t/t_{\text{end}} = 0.05, 0.25, 0.5, 1$, for the permeability field with Gaussian covariance function shown in Figure 1(b). (a) Mixed convection ratio 0, when there is no density contrast. (b) Mixed convection ratio 0.21. (c) Mixed convection ratio 0.42. (d)(e)(f) The time evolution of normalized pressure and concentration values at three data sampling points (marked by black circles in Figure 2(a)). The pressure values are normalized by the measured pressure value at $t = 0$, and the concentration values are normalized by the ambient solute concentration. Red line: data sampling point located at the first row, first column. Green line: data sampling point located at the third row, third column. Blue line: data sampling point located at the last row, last column.

Figure 3. Inversion results with PCGA for the Gaussian permeability field with $\sigma^2_{\ln k} = 0.25$. (a) True permeability field. (b) Estimated permeability field for passive tracer case, $M = 0$. (c) Estimated standard deviation for passive tracer case, $M = 0$. (d) Estimated permeability field for density-driven flow case, $M = 0.21$. (e) Estimated standard deviation for density-driven flow case, $M = 0.21$. (f) Estimated permeability field for density-driven flow case, $M = 0.42$. (g) Estimation standard deviation for density-driven flow case, $M = 0.42$.

Figure 4. Comparison between measured and estimated pressure data for the Gaussian permeability field shown in Figure 3. (a) $M = 0$. (b) $M = 0.21$. (c) $M = 0.42$.

Figure 5. Inversion results with PCGA for the exponential permeability field with $\sigma^2_{\ln k} = 0.25$. (a) True permeability field. (b) Estimated permeability field for passive tracer case, $M = 0$. (c) Estimation standard deviation for passive tracer case, $M = 0$. (d) Estimated permeability field for density-driven flow case, $M = 0.21$. (e) Estimation standard deviation for density-driven flow case, $M = 0.21$. (f) Estimated permeability field for density-driven flow case, $M = 0.42$. (g) Estimation standard deviation for density-driven flow case, $M = 0.42$.

Figure 6. Comparison between measured and estimated pressure data for the exponential permeability field shown in Figure 5. (a) $M = 0$. (b) $M = 0.21$. (c) $M = 0.42$.

Figure 7. (a) Residual sum of squares (RSS) between estimated and true *Gaussian* permeability fields for three different mixed convection ratios. We performed inversion for five different realizations for each mixed convection ratio. The filled symbols are RSS average over five realizations. (b) Residual sum of squares (RSS) between estimated and true *exponential* permeability fields for three different mixed convection ratios.

Figure 8. Residual sum of squares (RSS) between estimated and true tracer breakthrough curves for three different mixed convection ratios. The tracer breakthrough curves are measured at the 5×5 data sampling network. The filled symbols correspond to the RSS average over five realizations, and the error bars indicate one standard deviation. We observe that the transport predictability improves with the mixed convection ratio. (a) Gaussian permeability field. (b) Exponential permeability field.

Figure 9. Mapping accuracy of five different realizations for three different mixed convection ratios. The filled symbols correspond to the average mapping accuracy over five realizations. We observe that the mapping accuracy increases with the mixed convection ratio. (a) Gaussian permeability field. (b) Exponential permeability field.

Figure 10. Inversion results with PCGA for the Gaussian permeability field with $\sigma^2_{\ln k} = 0.5$. (a) True permeability field. (b) Estimated permeability field for passive tracer case, $M = 0$. (c) Estimation standard deviation for passive tracer case, $M = 0$. (d) Estimated permeability field for density-driven flow case, $M = 0.21$. (e) Estimation standard deviation for density-driven flow case, $M = 0.21$. (f) Estimated permeability field for density-driven flow case, $M = 0.42$. (g) Estimation standard deviation for density-driven flow case, $M = 0.42$.

Figure 11. Inversion results with PCGA for the exponential permeability field with $\sigma^2_{\ln k} = 0.5$. (a) True permeability field. (b) Estimated permeability field for passive tracer case, $M = 0$. (c) Estimation standard deviation for passive tracer case, $M = 0$. (d) Estimated permeability field for density-driven flow case, $M = 0.21$. (e) Estimation standard deviation for density-driven flow case, $M = 0.21$. (f) Estimated permeability field for density-driven flow case, $M = 0.42$. (g) Estimation standard deviation for density-driven flow case, $M = 0.42$.

Figure1.

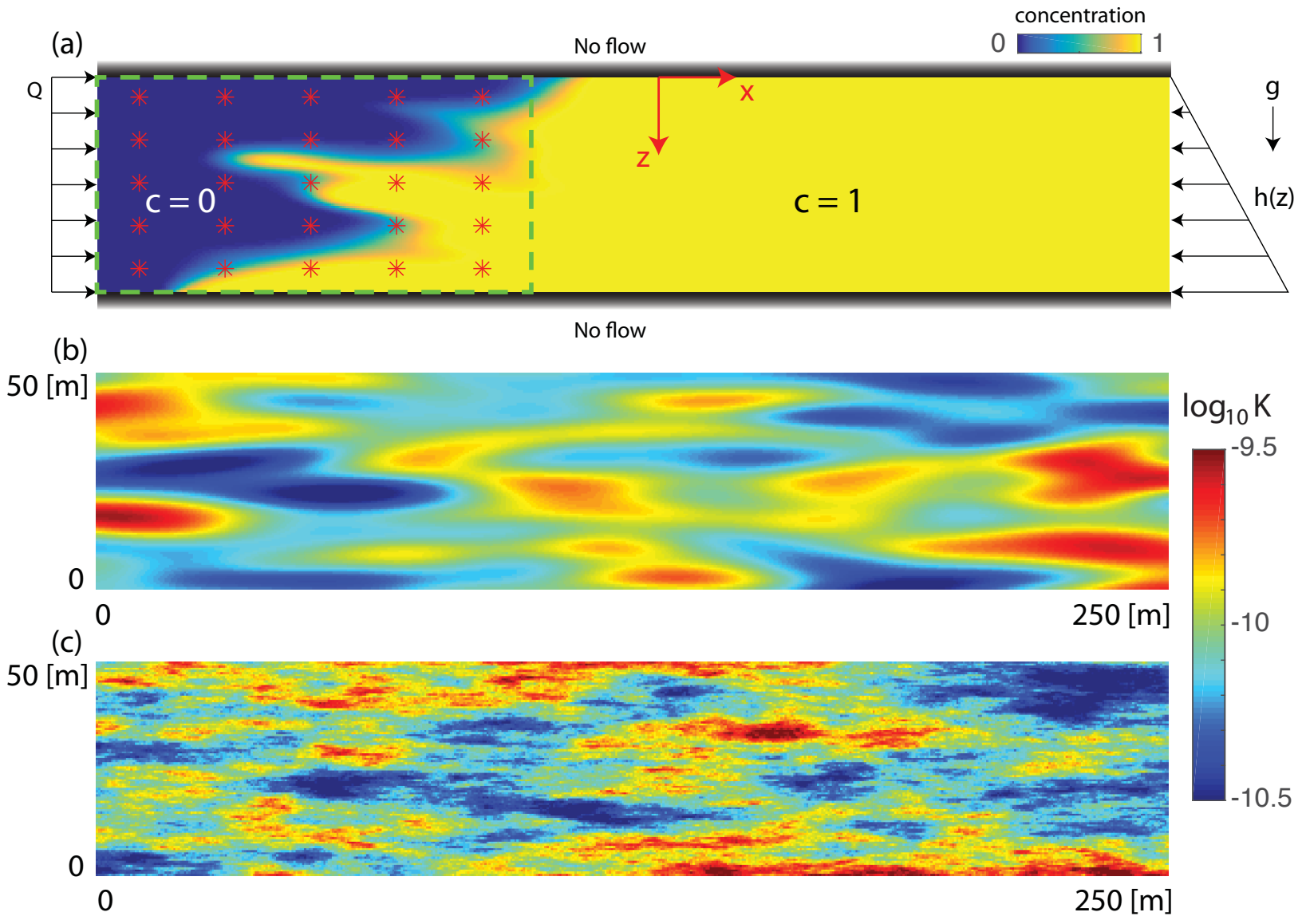
(a)
concentration
0
1
No flow
Q
x
z
g
h(z)
c = 0
c = 1
No flow
(b)
50 [m]
0
0
250 [m]
log10 K
-9.5
-10
-10.5
(c)
50 [m]
0
0
250 [m]

Figure2.

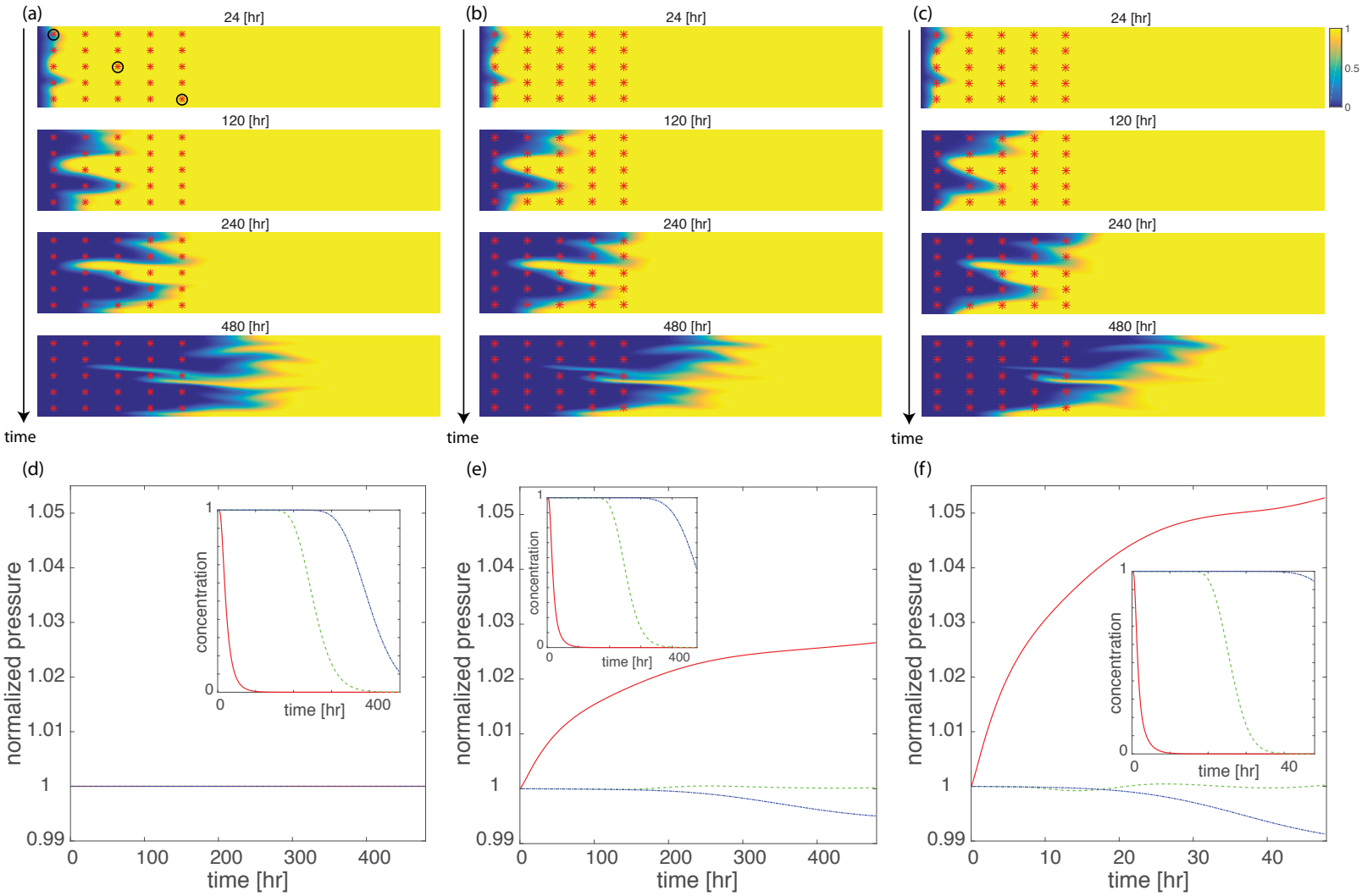
(a)
24 [hr]
120 [hr]
240 [hr]
480 [hr]
time
(b)
24 [hr]
120 [hr]
240 [hr]
480 [hr]
time
(c)
24 [hr]
120 [hr]
240 [hr]
480 [hr]
time
1
0.5
0
(d)
normalized pressure
time [hr]
concentration
time [hr]
(e)
normalized pressure
time [hr]
concentration
time [hr]
(f)
normalized pressure
time [hr]
concentration
time [hr]

Figure3.

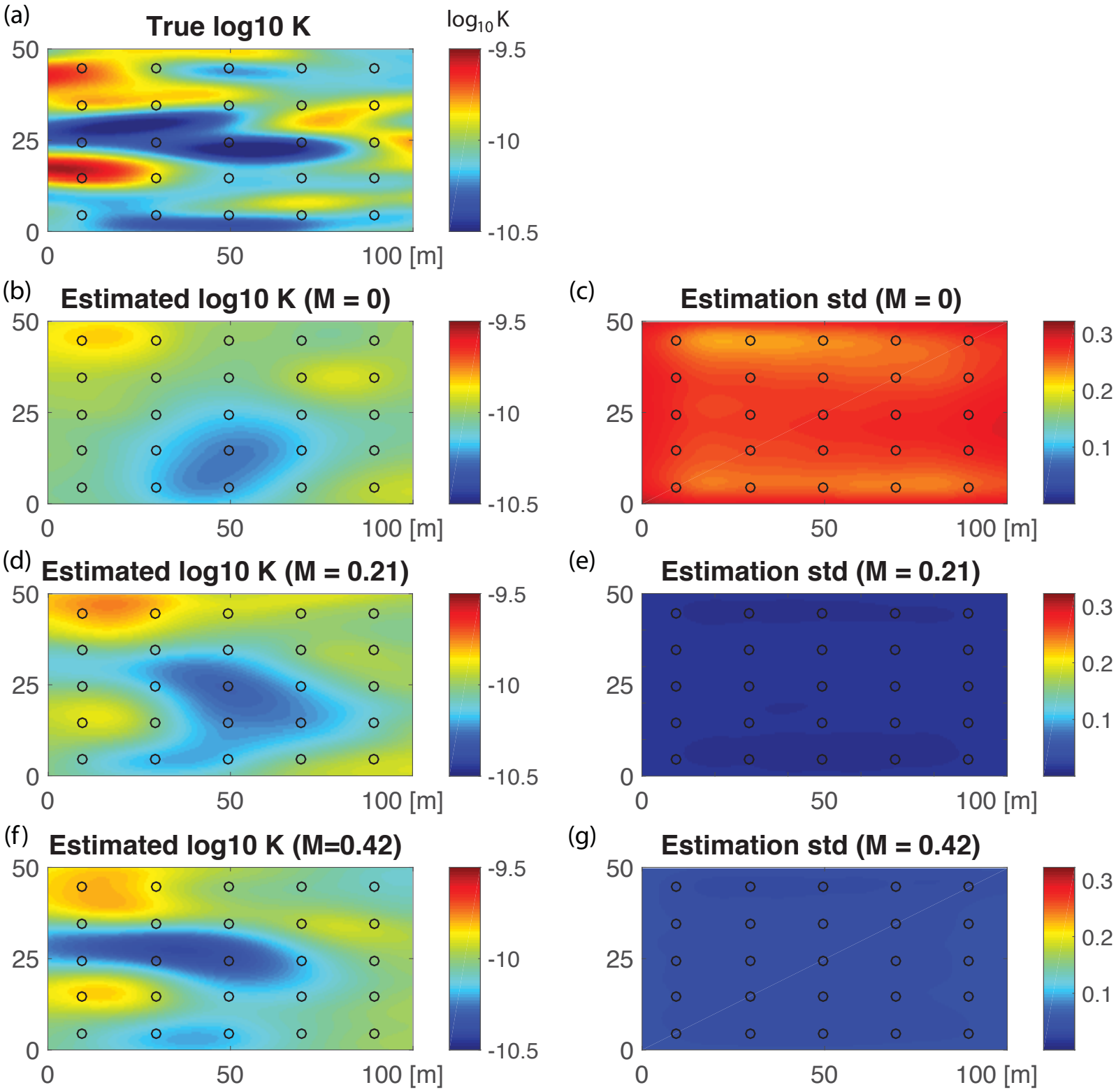
(a)
True log10 K
log10 K
50
25
0
0
50
100 [m]
-9.5
-10
-10.5
(b)
Estimated log10 K (M = 0)
(c)
Estimation std (M = 0)
0.3
0.2
0.1
(d)
Estimated log10 K (M = 0.21)
(e)
Estimation std (M = 0.21)
(f)
Estimated log10 K (M=0.42)
(g)
Estimation std (M = 0.42)

Figure4.

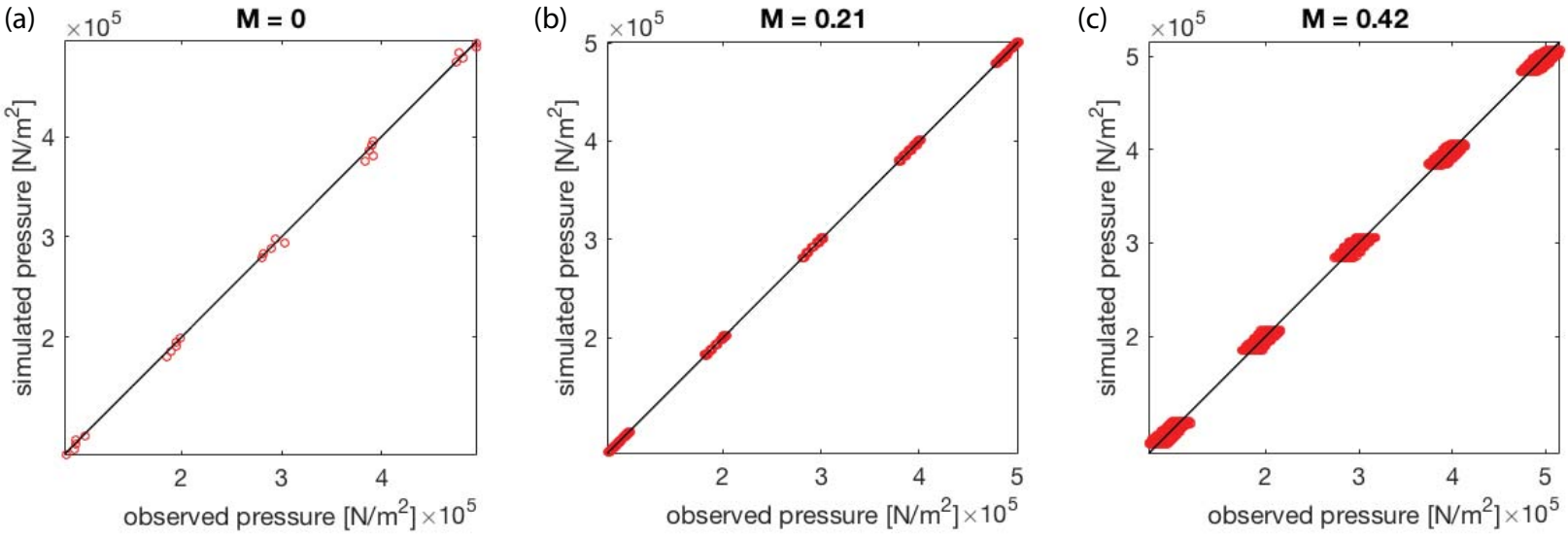
(a)
M = 0
(b)
M = 0.21
(c)
M = 0.42
×10^5
simulated pressure [N/m^2]
observed pressure [N/m^2] ×10^5
2
3
4
5

Figure5.

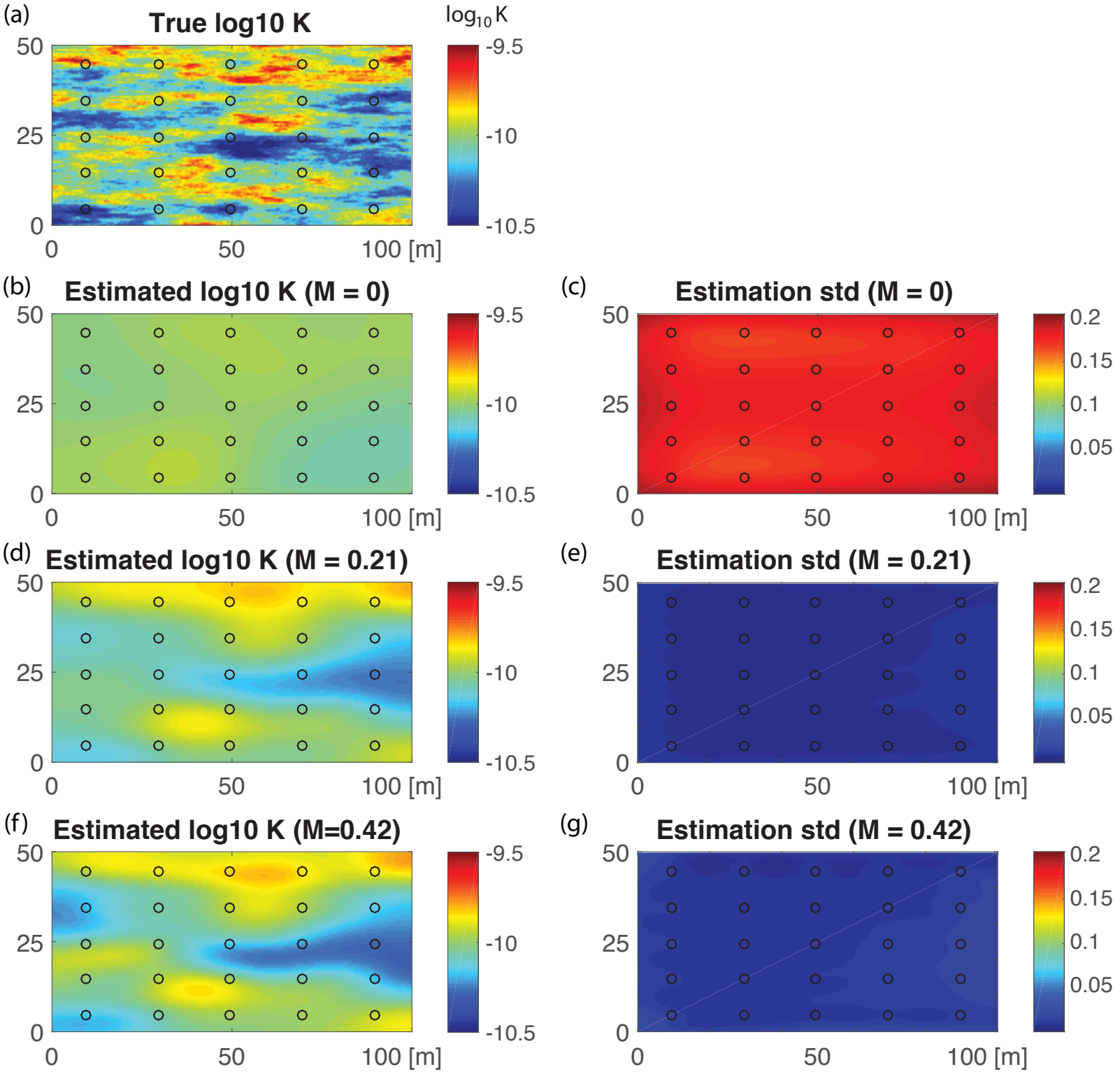
(a)
True log10 K
log10 K
50
25
0
0
50
100 [m]
-9.5
-10
-10.5
(b)
Estimated log10 K (M = 0)
(c)
Estimation std (M = 0)
0.2
0.15
0.1
0.05
(d)
Estimated log10 K (M = 0.21)
(e)
Estimation std (M = 0.21)
(f)
Estimated log10 K (M=0.42)
(g)
Estimation std (M = 0.42)

Figure6.

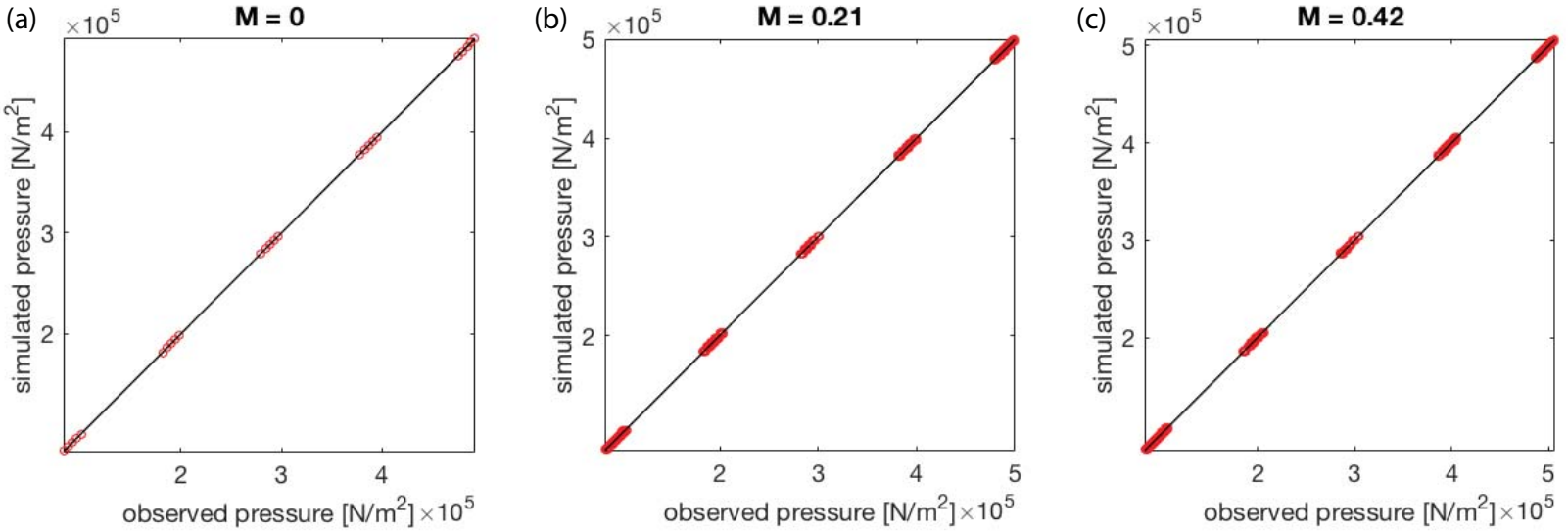
(a)
M = 0
(b)
M = 0.21
(c)
M = 0.42
×10^5
simulated pressure [N/m^2]
observed pressure [N/m^2] ×10^5
2
3
4
5

Figure7.

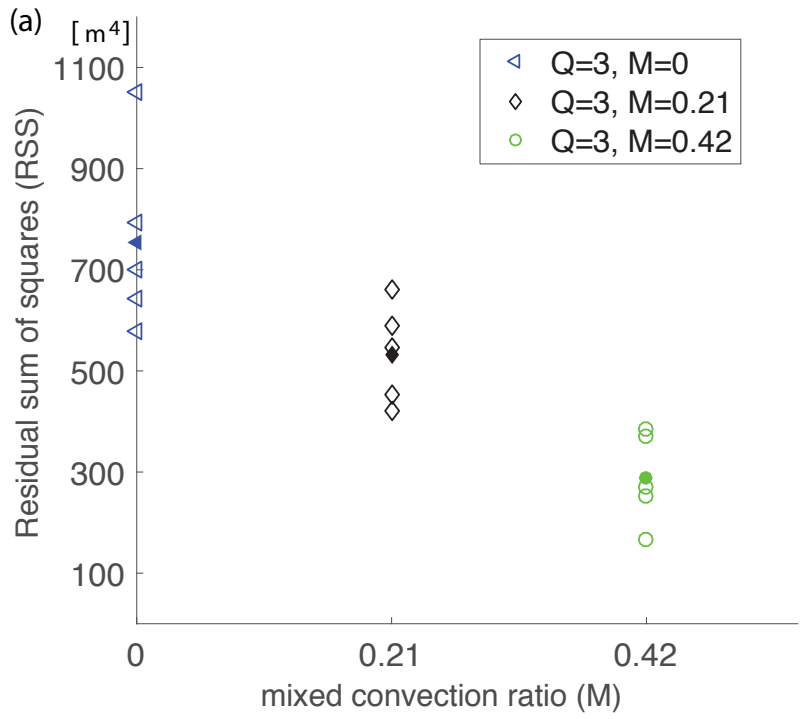
(a)
[m⁴]
1100
900
700
500
300
100
Residual sum of squares (RSS)
Q=3, M=0
Q=3, M=0.21
Q=3, M=0.42
0
0.21
0.42
mixed convection ratio (M)

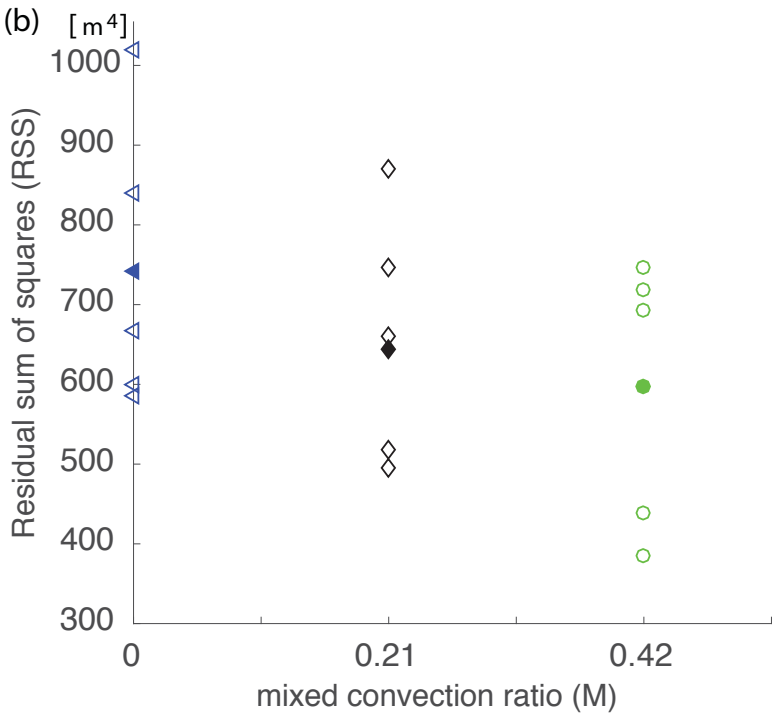
(b)
[m⁴]
1000
900
800
700
600
500
400
300
Residual sum of squares (RSS)
0
0.21
0.42
mixed convection ratio (M)

Figure8.

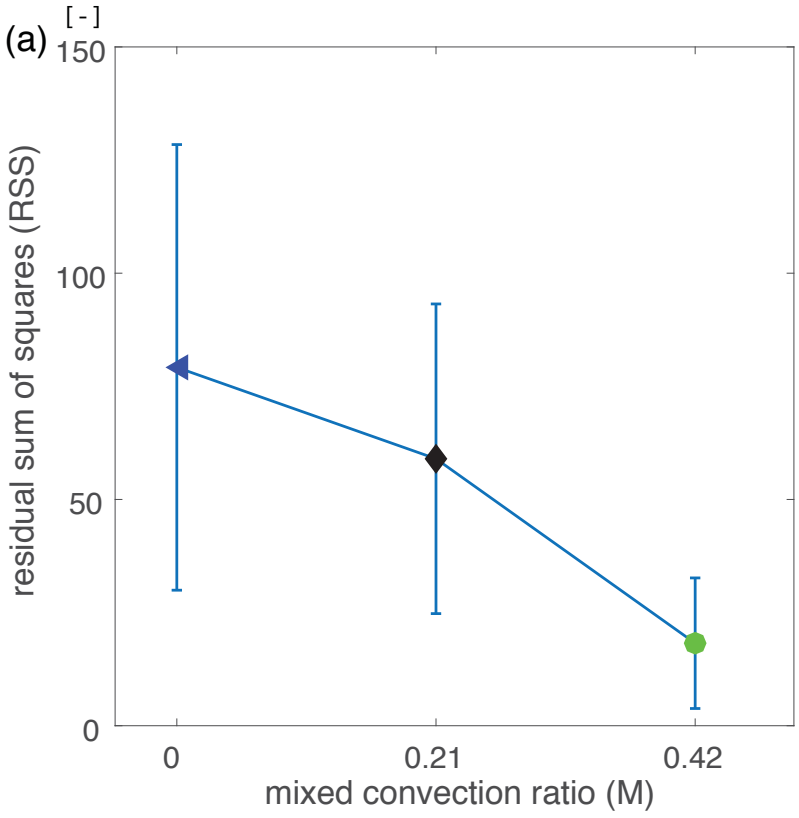
(a)
[-]
150
100
50
0
residual sum of squares (RSS)
0
0.21
0.42
mixed convection ratio (M)

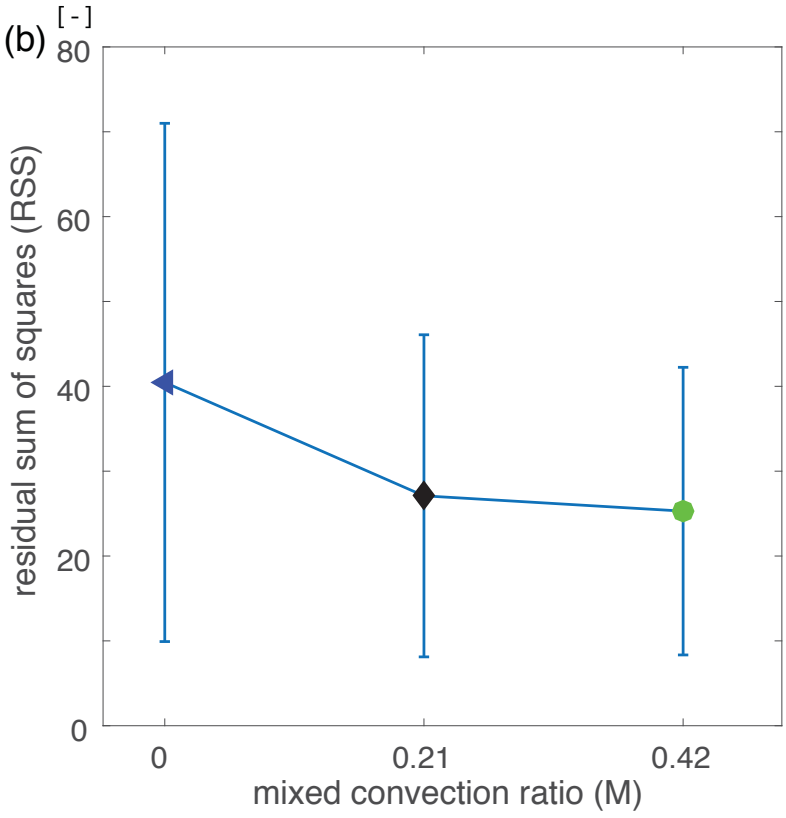
(b)
[-]
80
60
40
20
0
residual sum of squares (RSS)
0
0.21
0.42
mixed convection ratio (M)

Figure9.

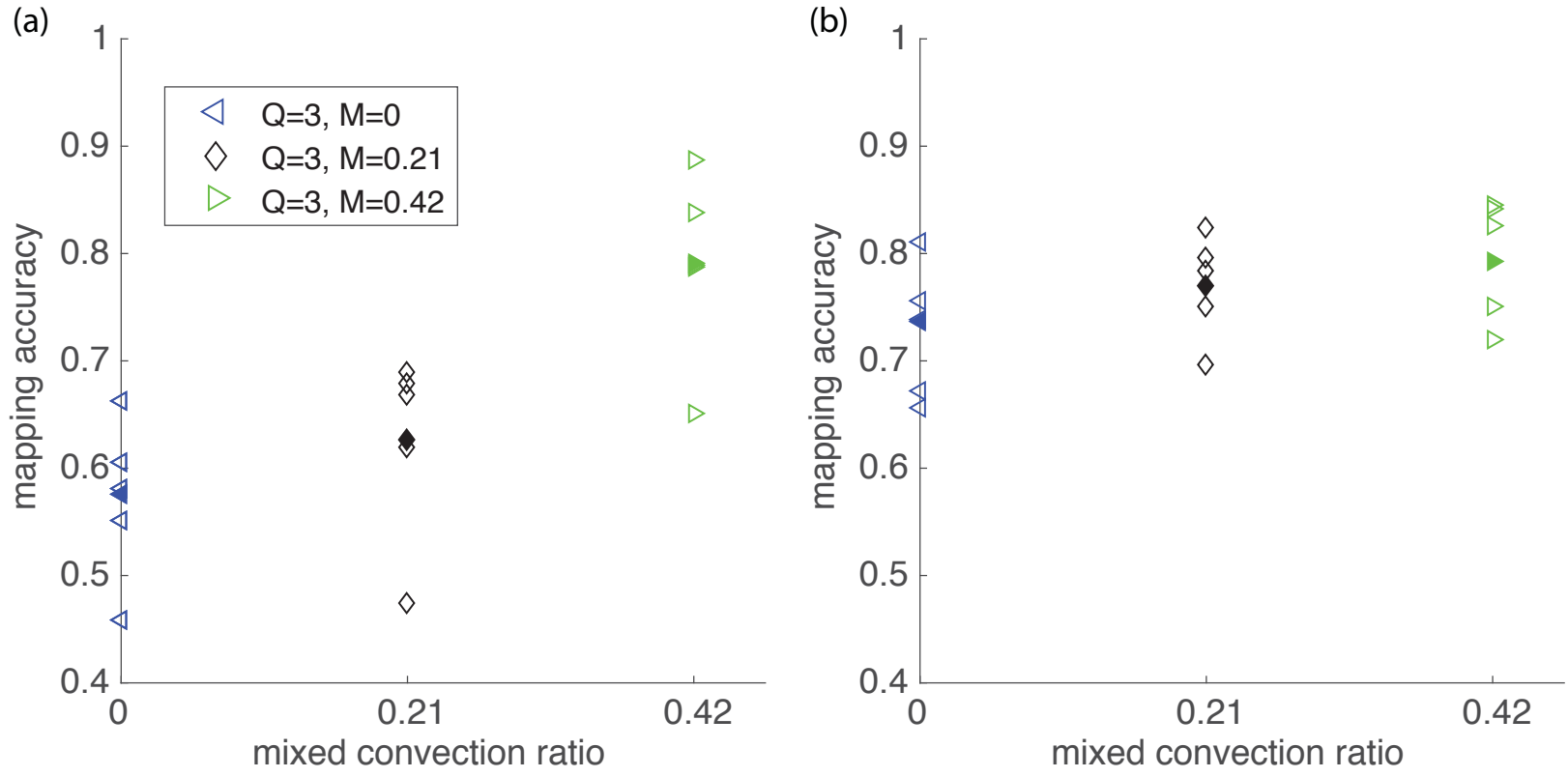
(a)
(b)
Q=3, M=0
Q=3, M=0.21
Q=3, M=0.42
mapping accuracy
mixed convection ratio
1
0.9
0.8
0.7
0.6
0.5
0.4
0
0.21
0.42

Figure10.

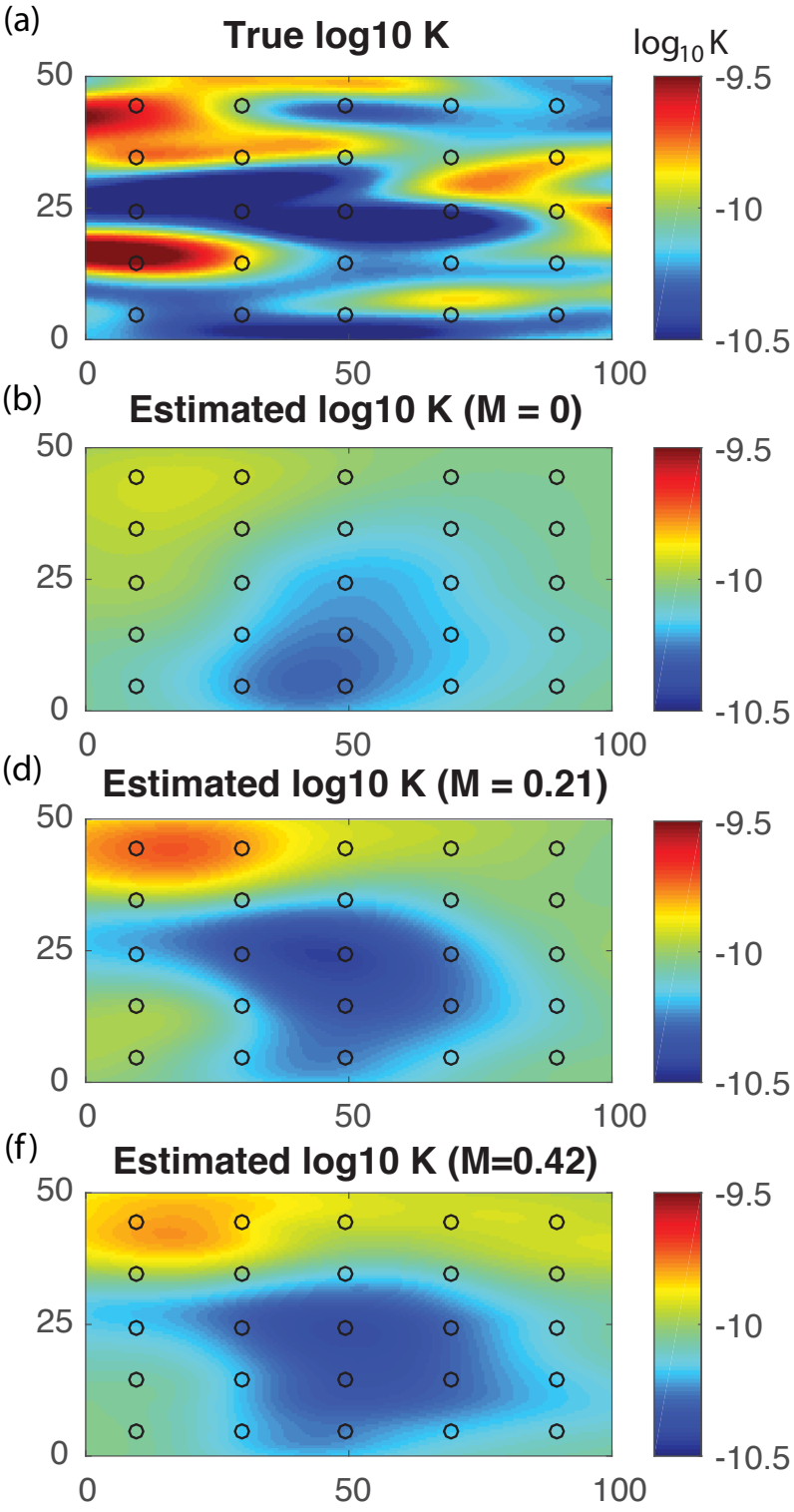
(a)
True log10 K
log10 K
50
25
0
0
50
100
-9.5
-10
-10.5
(b)
Estimated log10 K (M = 0)
(c)
Estimation std (M = 0)
0.2
0.1
(d)
Estimated log10 K (M = 0.21)
(e)
Estimation std (M = 0.21)
(f)
Estimated log10 K (M=0.42)
(g)
Estimation std (M = 0.42)

Figure11.

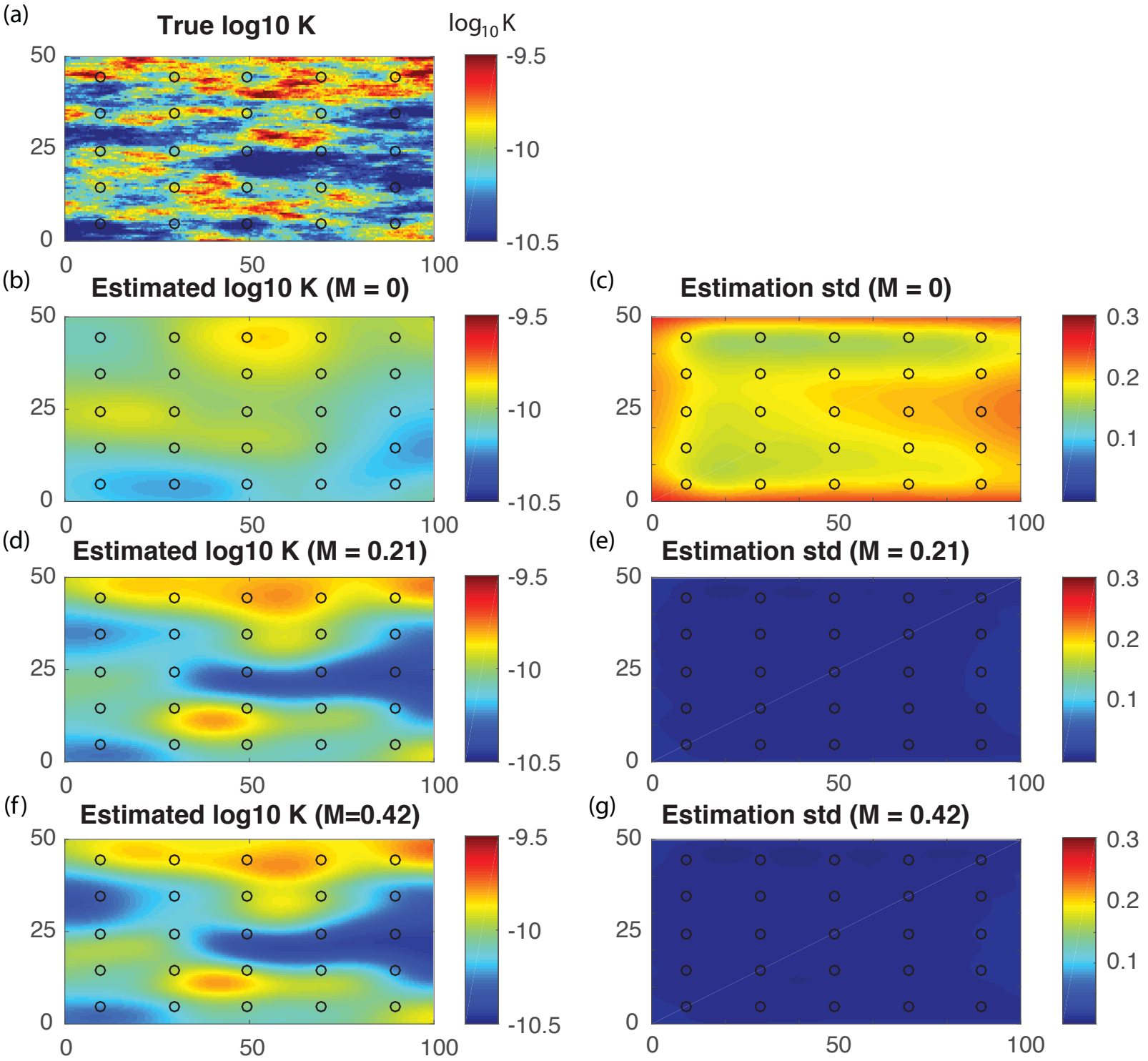
(a)
True log10 K
log10 K
-9.5
-10
-10.5
(b)
Estimated log10 K (M = 0)
(c)
Estimation std (M = 0)
0.3
0.2
0.1
(d)
Estimated log10 K (M = 0.21)
(e)
Estimation std (M = 0.21)
(f)
Estimated log10 K (M=0.42)
(g)
Estimation std (M = 0.42)
0
25
50
100